catalysts

MDPI

Article

High-Efficiency Catalytic Conversion of NO_x by the Synergy of Nanocatalyst and Plasma: Effect of Mn-Based Bimetallic Active Species

Yan Gao [1,2,3,*], Wenchao Jiang [1], Tao Luan [4,*], Hui Li [1,2,3], Wenke Zhang [1,2,3], Wenchen Feng [4] and Haolin Jiang [4]

1 Department of Thermal Engineering, Shandong Jianzhu University, Jinan 250101, China; jiang_wc@126.com (W.J.); lihui_sdjzu@sina.com (H.L.); zhangwk10@126.com (W.Z.)
2 Key Laboratory of Renewable Energy Building Utilization Technology of Ministry of Education, Shandong Jianzhu University, Jinan 250101, China
3 Key Laboratory of Renewable Energy Building Application Technology of Shandong Province, Shandong Jianzhu University, Jinan 250101, China
4 Engineering Laboratory of Power Plant Thermal System Energy Saving of Shandong Province, Shandong University, Jinan 250061, China; wcfeng18@126.com (W.F.); haolin_jiang@hotmail.com (H.J.)
* Correspondence: gaoyan.sdu@hotmail.com (Y.G.); prof.luantao@gmail.com (T.L.); Tel.: +86-138-6415-4887 (Y.G.); +86-175-1531-9316 (T.L.)

Received: 30 November 2018; Accepted: 16 January 2019; Published: 18 January 2019

Abstract: Three typical Mn-based bimetallic nanocatalysts of Mn−Fe/TiO_2, Mn−Co/TiO_2, Mn−Ce/TiO_2 were synthesized via the hydrothermal method to reveal the synergistic effects of dielectric barrier discharge (DBD) plasma and bimetallic nanocatalysts on NO_x catalytic conversion. The plasma-catalyst hybrid catalysis was investigated compared with the catalytic effects of plasma alone and nanocatalyst alone. During the catalytic process of catalyst alone, the catalytic activities of all tested catalysts were lower than 20% at ambient temperature. While in the plasma-catalyst hybrid catalytic process, NO_x conversion significantly improved with discharge energy enlarging. The maximum NO_x conversion of about 99.5% achieved over Mn−Ce/TiO_2 under discharge energy of 15 W·h/m^3 at ambient temperature. The reaction temperature had an inhibiting effect on plasma-catalyst hybrid catalysis. Among these three Mn-based bimetallic nanocatalysts, Mn−Ce/TiO_2 displayed the optimal catalytic property with higher catalytic activity and superior selectivity in the plasma-catalyst hybrid catalytic process. Furthermore, the physicochemical properties of these three typical Mn-based bimetallic nanocatalysts were analyzed by N_2 adsorption, Transmission Electron Microscope (TEM), X-ray diffraction (XRD), H_2-temperature-programmed reduction (TPR), NH_3-temperature-programmed desorption (TPD), and X-ray photoelectron spectroscopy (XPS). The multiple characterizations demonstrated that the plasma-catalyst hybrid catalytic performance was highly dependent on the phase compositions. Mn−Ce/TiO_2 nanocatalyst presented the optimal structure characteristic among all tested samples, with the largest surface area, the minished particle sizes, the reduced crystallinity, and the increased active components distributions. In the meantime, the ratios of $Mn^{4+}/(Mn^{2+} + Mn^{3+} + Mn^{4+})$ in the Mn−Ce/TiO_2 sample was the highest, which was beneficial to plasma-catalyst hybrid catalysis. Generally, it was verified that the plasma-catalyst hybrid catalytic process with the Mn-based bimetallic nanocatalysts was an effective approach for high-efficiency catalytic conversion of NO_x, especially at ambient temperature.

Keywords: NO_x conversion; DBD plasma; Manganese; bimetal; nanocatalyst

1. Introduction

Nitrogen oxides (NO_x) are regard as the main air pollutant contributing to acid rain, photochemical smog, greenhouse effects, and ozone depletion [1]. Selective catalytic reduction (SCR) of NO_x by NH_3 or urea is proposed to be the highly effective and completely developed method to eliminate NO_x pollution [2]. In coal fired power plants, the commercial catalyst of V_2O_5-$WO_3(MoO_3)/TiO_2$ is used for its excellent catalytic performance in the typical standard SCR reaction [3]:

$$4NO + 4NH_3 + O_2 \rightarrow 4N_2 + 6H_2O \quad (1)$$

While the $V_2O_5-WO_3(MoO_3)/TiO_2$ catalysts demand a strict temperature window of 300–400 °C, which limit the arrangement flexibility of this kind of catalyst. The vanadium-based catalysts can not reach satisfactory efficiency of eliminating NO_x when the reaction temperature is lower than 250 °C. In recent years, the fast selective catalytic reduction (fast SCR) attracted the attention of many research groups due to its lower reaction temperature and higher reaction efficiency [4]:

$$NO + NO_2 + 2NH_3 \rightarrow 2N_2 + 3H_2O \quad (2)$$

The catalysts appropriate to low temperature SCR are strongly desired, which could be located at downstream electrostatic precipitator and desulfurizer suitably [5]. However, the fast SCR still needs reaction temperature within 150–300 °C to achieve high efficiency of NO_x elimination [4,6]. Furthermore, the mole ratio of $NO:NO_2$ maintained at 1:1 is difficult in the real flue gas. Hence, it is necessary to develop an effective approach to eliminate NO_x with light concentration of NO_2 at low temperature region, which could be beneficial to the deNO_x device arrangement, as well as the SO_2 resistance.

Plasma-catalyst hybrid catalysis has been proved as an efficient technology to unite the high reactivity of plasma and the high selectivity of catalyst [7–9]. During the plasma-catalyst hybrid process, the plasma modifies not only the chemical properties and morphologies of the catalysts, but also changes the reaction pathway of an original catalytic process [10]. Plasma is confirmed to form an abundance of active species, such as O and O_3 radicals, which could oxidize NO into NO_2, further promoting catalysis via the fast SCR approach, especially at low temperature [4]. For the plasma-catalyst hybrid catalysis, the catalysts of $V_2O_5-WO_3/TiO_2$ [11], Ag/r-Al_2O_3 [12], Cu-ZSM-5 [13], and Mn−Ce/ZSM5−MWCNTs [4] have presented acceptable NO_x conversion efficiency under relatively low specific input energy. While the NO_x conversion maximum could still be further promoted at lower reaction temperature and smaller energy consume. Among the various transition metal elements applied in the catalysts for NO_x reduction, manganese displays superior activity especially at the low temperature, which can be attributed to the multifarious types of labile oxygen and high mobility of valence states [1]. Meanwhile, it has been found that iron, cobalt, and cerium species can combine with manganese to produce bimetallic catalysts, which contain abundant oxygen vacancies on the catalyst surface, forming strong interaction bands at atomic scale, such as Mn-O-Fe [14], Mn-O-Co [15], and Mn-O-Ce [16]. Moreover, the active metal species of FeO_x, CoO_x, and CeO_x are also regarded as the three typical promoters for NO_x conversion, which serve as core catalyst components of active metal oxides, supplying surface oxygen to accelerate NO_x elimination [14,15,17]. However, the effects of Mn-based bimetallic catalysts on the plasma-catalyst hybrid catalysis, especially the $Mn-Fe/TiO_2$, $Mn-Co/TiO_2$, and $Mn-Ce/TiO_2$ nanocatalysts have not been explored clearly.

In this study, we systematically synthesized three typical Mn-based bimetallic nanocatalysts of $Mn-Fe/TiO_2$, $Mn-Co/TiO_2$, and $Mn-Ce/TiO_2$. The synergistic effects of non-thermal plasma and Mn-based bimetallic nanocatalysts on NO_x catalytic conversion were investigated compared with the catalytic effects of plasma alone and nanocatalysts alone. Meanwhile, the influence factors of reaction temperature and discharge energy were taken into consideration during studying the synergetic mechanisms focusing on NO_x conversion of plasma and bimetallic nanocatalysts hybrid system. Furthermore, the physicochemical properties of these three typical Mn-based bimetallic nanocatalysts

were analyzed by Brunauer-Emmett-Teller (BET), transmission electron microscopy (TEM), X-ray diffraction (XRD), H_2-temperature-programmed reduction (TPR), NH_3-temperature-programmed desorption (TPD) and X-ray photoelectron spectroscopy (XPS), in order to expose the relationship between structures and activities. The purpose of this work was mean to explore the synergistic reinforcement mechanism of plasma-catalysis hybrid catalytic process over Mn-based bimetallic nanocatalysts for NO_x elimination with high catalytic efficiency and satisfied catalytic selectivity, especially at atmospheric temperature.

2. Results and Discussion

2.1. NO_x Conversion of Catalyst Alone Catalytic Process

The NO_x catalytic conversion and the catalytic selectivity of three typical Mn-based bimetallic nanocatalysts of Mn−Fe/TiO_2, Mn−Co/TiO_2, and Mn−Ce/TiO_2 were exhibited in Figure 1, and the catalytic ability of Mn/TiO_2 catalyst was also depicted as a contrast. For all the tested Mn-based bimetallic nanocatalysts, the NO_x conversion increased significantly with the temperature rising from 25 °C to 250 °C and presented excellent performance (>90%, above 150 °C). Compared with the Mn/TiO_2 catalyst, the catalytic activities of Mn-based bimetallic nanocatalysts were remarkably improved at the whole temperature range, potentially due to the strong interaction of Mn−O−X bond (X refered to Fe, Co or Ce), the improvement of Brønsted acid sites and Lewis acid sites, and the enhancement of Eley-Rideal (E-R) mechanism reaction [18], which could be further verified by the following physicochemical properties. As shown in Figure 1a, Mn−Ce/TiO_2 nanocatalyst achieved higher catalytic activity than the other samples in the temperature range of 25~200 °C. The Mn−Fe/TiO_2 nanocatalyst showed the minimum NO_x conversion among these three Mn-based bimetallic nanocatalysts, while still much larger than that of Mn /TiO_2 sample. However, the catalytic selectivity of Mn−Fe/TiO_2 nanocatalyst was lower than that of Mn−Co/TiO_2 and Mn−Ce/TiO_2 within 175~250 °C, as exhibited in Figure 1b. Furthermore, it could be easy to find there was no obvious difference of NO_x conversion or catalytic selectivity over these three Mn-based bimetallic nanocatalysts at ambient temperature, which was proposed to be due to the low catalytic activities for all the tested catalysts.

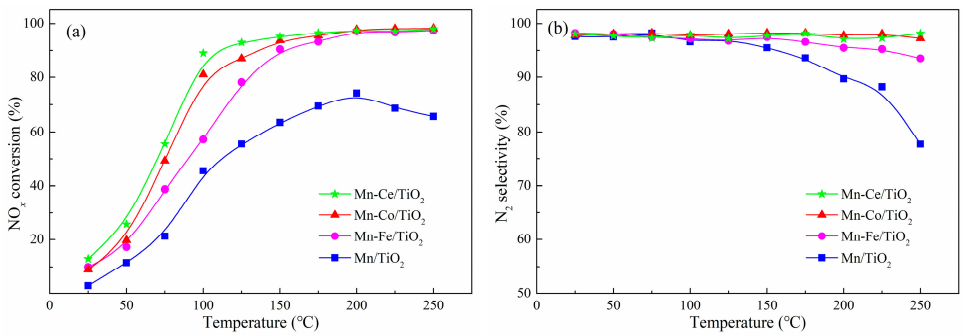

Figure 1. Catalytic performance of catalysts without plasma. Gas mixture composition: 300 ppm NO, 300 ppm NH_3, 8% O_2, ~0.1% H_2O and N_2 as balance gas. Gas hourly space velocity (GHSV) 20,000 h^{-1}. (**a**) NO_x conversion of Mn-based nanocatalysts; and (**b**) N_2 selectivity of Mn-based nanocatalysts.

2.2. NO_x Conversion of Plasma-Catalyst Hybrid Catalytic Process

The NO conversion and NO_2 concentration over three typical Mn-based bimetallic nanocatalysts were compared in Figure 2. The performance of all prepared nanocatalysts were measured in terms of various discharge energies to reveal the interaction of Mn−O−Fe, Mn−O−Co, and Mn−O−Ce. As shown in Figure 2a, both Mn−Co/TiO_2 and Mn−Ce/TiO_2 nanocatalysts could reach NO_x conversion maximum >99% within the discharge energy range of 18~24 W·h/m^3. While the start discharge energy of Mn−Ce/TiO_2 nanocatalyst with superior SCR activities was much lower than

that of Mn−Co/TiO_2nanocatalyst. The Mn−Ce/TiO_2 bimetallic nanocatalyst raised the optimal NO_x conversion to 93.3% with the relatively low discharge energy of 12 W·h/m^3. For the other Mn-based bimetallic nanocatalysts, a lower NO_x elimination efficiency was achieved with NO_x conversion less than 85% at 15 W·h/m^3 and the maximum obtained at 24 W·h/m^3, which meant that the higher discharge energy was required to induce the plasma-catalyst catalytic process, and the narrower discharge energy window was limited to the hybrid catalytic reaction.

The N_2 and O_2 contained in the gas mixture were motivated to form N and O atoms via the collision of active electrons in the plasma-catalyst hybrid system. Compared to the chemical-bond dissociation energies of N_2 (945.33 kJ/mol), the O_2 was much easier to react with the energetic electrons for its lower chemical-bond dissociation energies of 498.36 kJ/mol. As a result, a high concentration of O radicals was produced in the plasma-catalyst system. The generated dominating O radicals and subordinate N radicals could react with NO/O_2/N_2/NH_3 gas mixture in the following reactions (3)~(8) [19]. The oxidation reactions (5) and (6) occurred between the radicals of O and O_3 and the NO molecules to generate NO_2 were regarded as the positive main steps to enhance NO conversion [7,9].

$$O + O_2 \rightarrow O_3 \tag{3}$$

$$O_3 + NO \rightarrow NO_2 + O_2 \tag{4}$$

$$O + NO \rightarrow NO_2 \tag{5}$$

$$O + NO_2 \rightarrow NO + O_2 \tag{6}$$

$$O + N \rightarrow NO \tag{7}$$

$$NO + N \rightarrow N_2 + O \tag{8}$$

Thus, in the plasma-catalyst hybrid catalytic process, the catalytic reactions (2) and (3) become the predominant paths for NO elimination [4]. It had been testified that the reaction rate of fast SCR reaction (2) was more than 10 times larger than that of standard SCR reaction (1) below 200 °C [17].

Meanwhile, the NO_2 concentrations over Mn-based bimetallic nanocatalysts were relatively lower compared to that of plasma without catalyst assistance. Under discharge energy of 24 W·h/m^3, more than 120 ppm NO_2 generated in the plasma-only catalytic process. However, the NO_2 concentration in Mn-based bimetallic nanocatalysts combining with plasma was no more than 20 ppm, which indicated that almost 100 ppm NO_2 took part in the catalytic reaction probably via the fast SCR reaction or the catalytic oxidation, as shown in Figure 2b. Therefore, it was believed that both the fast SCR and the standard SCR reactions occurred in the plasma-catalyst hybrid system simultaneity and the proportion of NO_x conversion via the fast SCR reaction improved with the discharge energy increasing. The N_2 selectivity over the Mn-based nanocatalysts was displayed in Figure 2c. The N_2 selectivity of the plasma-catalyst hybrid catalytic process was obviously larger than that of plasma-only process within discharge energy range of 0~24 W·h/m^3, which was owing to the possibility of higher NO conversion and lower NO_2 formation, discussed above in Figure 2a,b. All test results presented a decreasing trend of N_2 selectivity with the discharge energy rising, which resulted from a great deal of N_2O produced in this reaction operation. It was proposed that the pivotal disadvantages of catalyzing NO_x by plasma were the low selectivity and the complex chemical productions that formed via diverse reaction pathways [10]. In order to verify the actual reactions during the plasma-catalyst hybrid process over the Mn-based bimetallic nanocatalysts, the NO_x conversion and the N_2 selectivity over Mn−Ce/TiO_2 sample in the balance gas of N_2 and Ar were tested, as shown in Figure 2d. It was obvious that the variation tendency of NO_x conversion obtained in the balance gas of N_2 and Ar were quite similar. While within the whole discharge energy range of 0~24 W·h/m^3, the NO_x conversion in Ar was slightly higher. According to a previous report, under abundant O radicals or O_2, the N species is ten times more likely to react with O_2 than with NO [20]. Hence, almost N atoms produced from N_2 in the plasma transformed to NO via reaction (7), which was further oxidized into NO_2 and eliminated

via fast SCR reactions immediately [7]. Therefore, in the balance gas of N_2, the NO concentration formed from N and O radicals was relatively small compare to the initial NO_x concentration, which caused little influence on the NO_x conversion during the plasma-catalyst hybrid process. Meanwhile, there was no obvious difference between the N_2 selectivity obtained in the balance gas of N_2 and Ar. The NO_x conversions over Mn−Ce/TiO_2 nanocatalyst with and without O_2 were analyzed as exhibited in Figure 2e. The NO_x conversion decreased drastically from 99.1% to 43% with the O_2 concentration dropping from 8% to 0%, which demonstrated the oxidation pathway for NO reduction by O species via reactions (3), (4), and (5) was dominant during the plasma-catalyst hybrid process. The NO_x conversions under O_2 8% and 4% were almost the same, indicating the amount of oxygen excessive for NO_x redox reactions. Due to the dissociation energy of O_2 much smaller than that of N_2, the rate for dissociation of O_2 was much higher compared to the dissociation of N_2, which was the main reason for the remarkable promotion of O_2 on NO_x conversion [21].

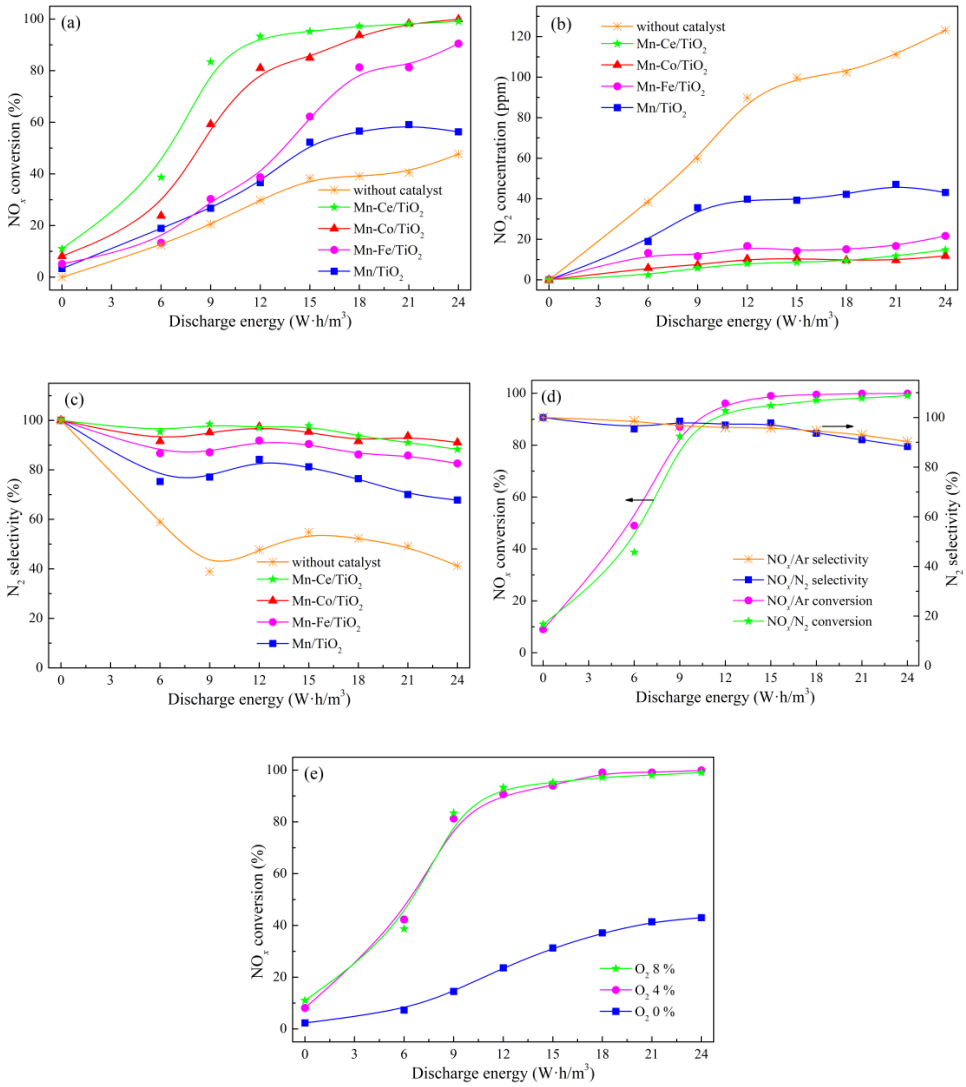

Figure 2. Catalytic performance of plasma-catalyst hybrid catalytic process at ambient temperature. Gas mixture composition: 300 ppm NO, 300 ppm NH_3, 8% O_2, ~0.1% H_2O, and N_2/Ar as balance gas. Gas hourly space velocity (GHSV) 20,000 h^{-1}. (**a**) NO_x conversion; (**b**) NO_2 concentration; (**c**) N_2 selectivity; (**d**) NO_x conversion and N_2 selectivity in balance gas of N_2 and Ar over Mn−Ce/TiO_2; and (**e**) NO_x conversion over Mn−Ce/TiO_2 with and without O_2.

The interaction effects of discharge energy and temperature on NO_x conversion in plasma with and without Mn-based bimetallic nanocatalysts reaction process were shown in Figure 3. The variation

tendency of NO_x conversion in plasma-only process was opposite to that in plasma-catalyst hybrid process with reaction temperature increasing. As displayed in Figure 3a, high reaction temperature led to significant reduction in NO_x elimination, with the maximum catalytic conversion of 49.5% at 21 W·h/m^3, 25 °C declining to 20.5% at 12 W·h/m^3, 200 °C. In the plasma catalytic process, the NO_2 generation via interaction between the radicals of O and O_3 and the NO molecules was conducive to deNO_x as analyzed above. While with the formed NO_2 accumulation in the plasma-only process, the inhibition of reaction (6) on NO elimination progressively intensified. The concentration of O radical could be improved under high temperature, which could further promote reaction (5), (6), and (7). As a result, the temperature increase spurred the formation of NO and impeded NO oxidation into NO_2 [19]. Considering the energy consume during the plasma-catalyst process, the reaction temperature in the catalyst bed could be higher than the outside of nanocatalysts. In order to clearly realize the relation between reaction temperatures and plasma, an infrared thermometer was introduced to detect the specific temperature of discharge area during the plasma process. The test results were shown in Figure 3b. The plasma energy caused the temperature of the discharge area improved at different degrees and the largest temperature increase could reach 47 °C under the discharge energy of 24 W·h/m^3. While the reaction temperature of gas mixture influenced by the plasma energy was relatively smaller with the Maximum temperature rise no larger than 13 °C, due to the short residence time of the gas mixture in the discharge area. Therefore, under the experiment conditions of this research, the plasma effects on NO conversion could be primarily analyzed by the discharge energy based on the gas mixture temperature.

It was apparent that the trends of NO conversion of these three Mn-based bimetallic nanocatalysts were consistent, as exhibited in Figure 3c–e). The NO conversion under different reaction temperatures and various discharge energies could be divided into three zones. In zone I, the NO_x conversion >90% only depended on the discharge energy and not affected by the reaction temperature. In zone II, the satisfied NO_x conversion (>90%) was achieved and both depended on the discharge energy and the reaction temperature. In zone III, it was impossibility to acquire a desired NO_x conversion. Mn−Ce/TiO_2 nanocatalyst presented superior catalytic property than Mn−Co/TiO_2 and Mn−Fe/TiO_2 samples with much broader zone I, which signified high NO_x conversion obtained with lower reaction temperature and the less discharge energy. A variety of previous works had revealed the optimal NO_x conversions obtained with the specific input energy varying from 4.7 to 40.3 W·h/m^3 and the temperature changing from 25 to 350 °C, as shown in Table 1. In this study, Mn−Ce/TiO_2 sample exhibited the superior performance with NO_x conversion of 99.5% under 15 W·h/m^3 at 25 °C, respectively, which was believed to be a potential excellent catalyst for the NO removal via the plasma-catalyst process.

Table 1. Plasma-catalyst performance in previous researches.

Samples	Specific Input Energy (W·h/m^3)	NO_x Conversion (%)	Temperature (°C)	Reductant	GHSV (h^{-1})	Gas Flow Rate (m^3/h)	Ref
V_2O_5-WO_3/TiO_2	4.7 [a]	~76.5	170	NH_3	–	31.8	[11]
H-mordenite	5	76	160	NH_3	20,000	31	[7]
Ag/Al_2O_3	16.7 [a]	~91	350	C_3H_6	10,000	1.2	[12]
$BaTiO_3$-Al_2O_3	~40.3 [a]	~61.5	150	CH_3OH	11,000	–	[22]
Cu-ZSM-5	37.5 [a]	~90	25 [b]	C_2H_4	–	0.12	[13]
Co-ZSM-5	8.3 [a]	~70.6	150	C_2H_4+NH_3	1000	0.12	[22]
Co-HZSM-5	38.3	~92	300	C_2H_2	12,000	0.03	[23]
Mn−Ce/ZSM5−MWCNTs	16.7 [a]	~85	25	NH_3	60,000	0.12	[4]
Mn−Ce/TiO_2	15	99.5	25	NH_3	20,000	0.1	This study

[a] calculated according to the data in the report (1 W·h/m^3 = 3.6 J/L); [b] room temperature.

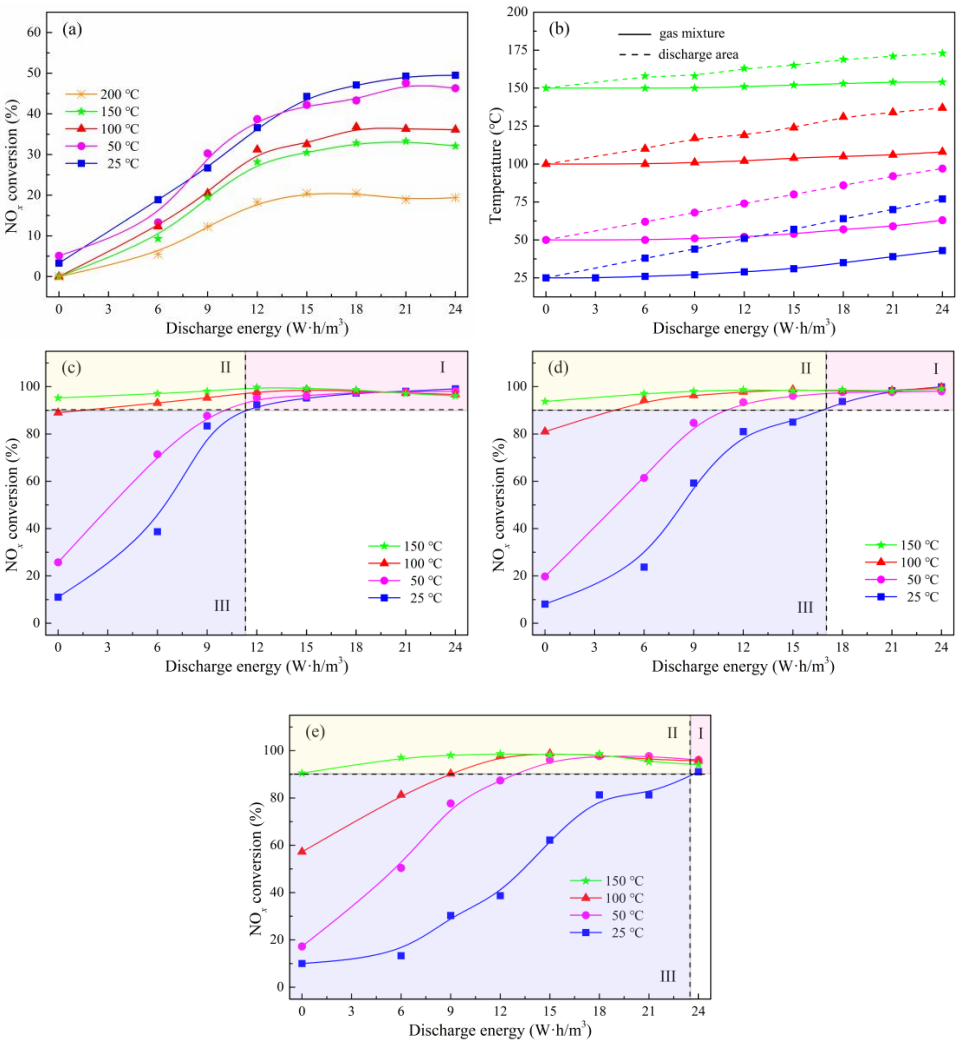

Figure 3. Effect of temperature on NO conversion. Gas mixture composition: 300 ppm NO, 300 ppm NH_3, 8% O_2, ~0.1% H_2O, and N_2 as balance gas. Gas hourly space velocity (GHSV) 20,000 h^{-1}. (**a**) plasma-only process; (**b**) plasma cooperate with Mn−Ce/TiO_2 nanocatalysts; (**c**) plasma cooperate with Mn−Co/TiO_2 nanocatalysts; and (**d**) plasma cooperate with Mn−Fe/TiO_2 nanocatalysts.

2.3. Morphological Characterization

2.3.1. BET Measurements

In order to achieve the physical properties of these three typical Mn-based bimetallic nanocatalysts, the results of specific surface areas (S_{BET}), total pore volumes (V_{total}), and average pore diameters (D_p) were summarized in Table 2. It was evident that Mn−Ce/TiO_2 nanocatalyst obtained larger specific surface areas than Mn−Co/TiO_2 nanocatalyst and was more than twice as much as Mn−Fe/TiO_2 nanocatalyst, which was probable, owing to the Mn−Ce−O_x species better dispersed on the nanocatalyst surface. Meanwhile, there were noticeable changes of D_p, increasing from 17.57 nm in Mn−Ce/TiO_2 to 33.06 nm in Mn−Co/TiO_2 and further rising to 54.85 nm in Mn−Fe/TiO_2. It was proposed that the Mn−Ce−O_x species were more likely to promote nanocatalyst to form micropores compared with Mn−Co−O_x and Mn−Fe−O_x species [24,25]. However, the difference of total pore volumes among these three Mn-based bimetallic nanocatalysts was not obvious. The total pore volumes of Mn−Ce/TiO_2 and Mn−Co/TiO_2 samples centered on 0.53 $cm^3 \cdot g^{-1}$, approximately. While the total pore volume of Mn−Fe/TiO_2 decreased to 0.424 $cm^3 \cdot g^{-1}$ slightly, which was probable due to the mesoporosity formation that suppressed the micropore generation, resulting in the total pore

volume reduced a little. Thereby, it was believed that Mn−Ce/TiO_2 nanocatalyst had superior physical properties than the other two samples with larger specific surface area, more micropores structure and satisfied total pore volumes, which coincided with catalytic performance of catalysts without plasma, as shown in Figure 1.

Table 2. Physical properties of Mn-based bimetallic nanocatalysts.

Samples	S_{BET} ($m^2 \cdot g^{-1}$)	V_{total} ($cm^3 \cdot g^{-1}$)	D_p (nm)
Mn−Ce/TiO_2	239.7	0.527	17.57
Mn−Co/TiO_2	189.9	0.531	33.06
Mn−Fe/TiO_2	104.6	0.424	54.85

2.3.2. TEM Analysis

The morphological characterization and grain structure of these three typical Mn-based bimetallic nanocatalysts were collected by TEM analysis. From Figure 4a, it could be observed that Mn−Ce/TiO_2 nanocatalyst was constituted of fine uniform nanoparticles with narrow size distribution, smooth elliptic surfaces, and without evident agglomeration. The distinct and unbroken mesh structure of micropore was formed in the Mn−Ce/TiO_2 sample. According to the TEM images of Mn−Co/TiO_2 nanocatalyst, as shown in Figure 4b, there were some tightly aggregated metal oxide nanoparticles interfused into the smaller regular particles, which increased the average pore diameters and reduced the specific surface areas to some extent. However, from Figure 4c, a noticeable augment in the particle size was observed over Mn−Fe/TiO_2 nanocatalyst, which was consistent with Barrett–Joyner–Halenda (BJH) results. The nanoparticles were irregular, lots of which stacked on the catalyst surface with an abundant micropore structure collapsing and regional accumulations.

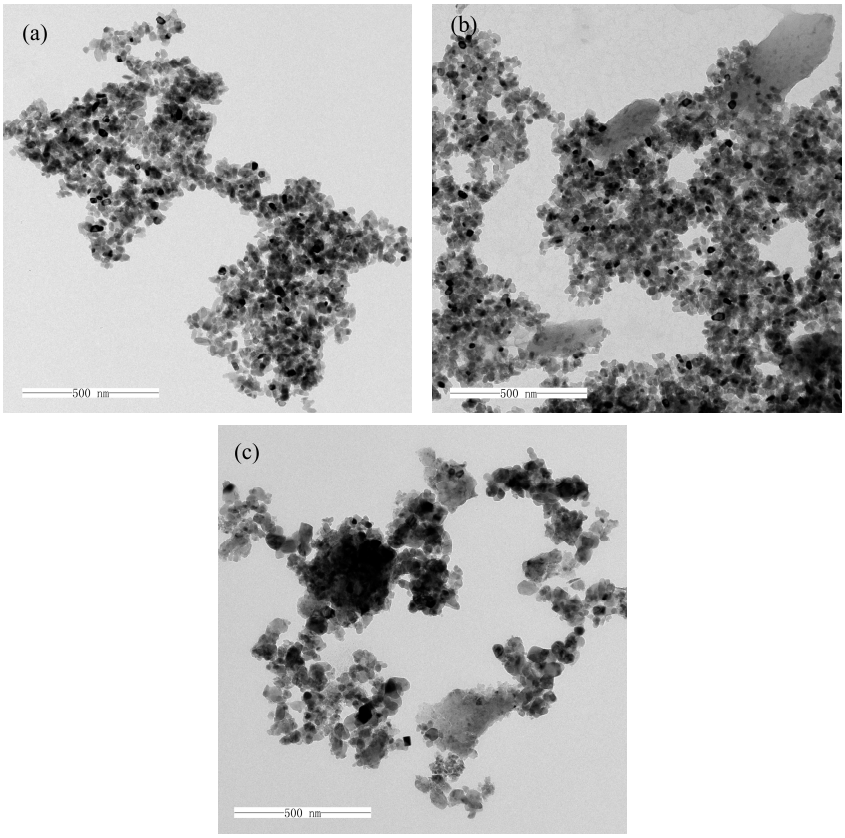

Figure 4. TEM of Mn-based bimetallic nanocatalysts. temperature on NO conversion. (**a**) Mn−Ce/TiO_2; (**b**) Mn−Co/TiO_2; and (**c**) Mn−Fe/TiO_2.

2.4. Structural Characterization

2.4.1. Textural Properties

Figure 5a exhibited the XRD spectra of Mn-based bimetallic nanocatalysts and the phases contained in the nanocatalyst samples were identified by the software of MDI Jade 6.5. Among all these three nanocatalysts, there were strong and distinguished diffraction peaks at about 2θ values of 25.3°, 37.8°, 48.0°, 53.9°, 62.7°, 68.8°, 70.3°, 75.1°, and 82.7° well matched the XRD pattern of anatase TiO_2 (ICDD PDF card # 71-1166) [26]. While the diffraction peaks for the structure of TiO_2 support were reserved completely, the diffraction angles of the matching peaks shifted at different degrees. In Mn−Ce/TiO_2 nanocatalyst, the anatase TiO_2 presented the lowest diffraction angle for every corresponding peak, which probably verified the interaction between $MnCeO_x$ and anatase TiO_2 was stronger than that between $MnCoO_x$ or $MnFeO_x$ and anatase TiO_2. Comparing these three nanocatalysts, it could be found that the diffraction peaks of anatase TiO_2 in Mn−Ce/TiO_2 nanocatalyst were broader and weaker than that in the other two nanocatalysts, indicating the crystalline of TiO_2 reduced by the $MnCeO_x$ loading. Meanwhile, there was no obvious characterization reflections for MnO_x or CeO_x in Mn−Ce/TiO_2 nanocatalyst that manifested the active species were finely dispersed on the nanocatalyst surface or the active species of MnO_x and CeO_x incorporated into TiO_2 lattice [27].

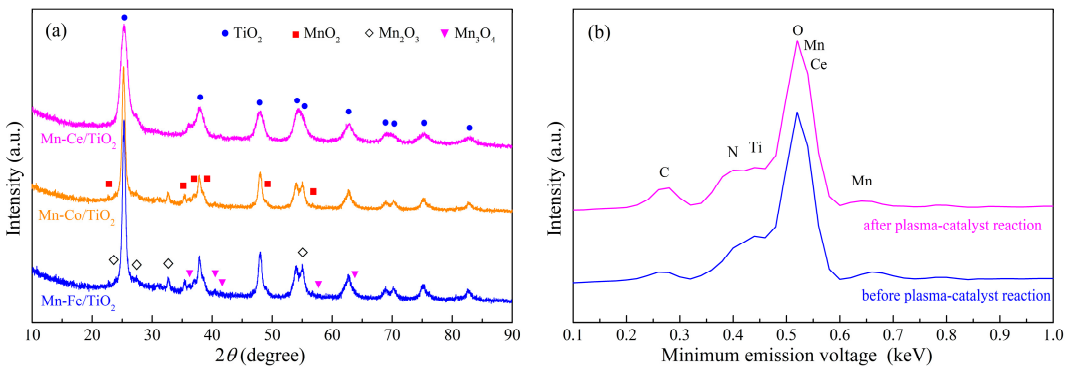

Figure 5. XRD patterns of Mn-based bimetallic nanocatalysts and element contents of Mn−Ce/TiO_2 before and after plasma-catalyst reaction. (**a**) XRD patterns of Mn−Ce/TiO_2, Mn−Co/TiO_2 and Mn−Fe/TiO_2 nanocatalysts; and (**b**) EDS patterns of element contents on the surface of Mn−Ce/TiO_2.

In the XRD patterns of Mn−Co/TiO_2 and Mn−Fe/TiO_2 nanocatalysts, the diffraction peaks accord with MnO_x were very complex due to the transformation among MnO_2, Mn_2O_3, Mn_3O_4, and MnO in the incomplete crystallization of manganese oxides. The diffraction peaks matched with MnO_2 exactly at 2θ = 22.10°, 35.19°, 36.96°, 38.72°, 47.86°, and 57.166°, corresponding to the crystallographic plane reflections of (110), (310), (201), (111), (311), and (420), respectively (ICDD PDF card # 82-2169) [28]. At the same time, the diffraction peaks of Mn_2O_3 and Mn_3O_4 were evident in Mn−Co/TiO_2 and Mn−Fe/TiO_2 nanocatalysts. The intensive and sharp characteristic peaks at 2θ values of 23.08°, 26.72°, 32.87°, and 56.89° could be primarily ascribed to Mn_2O_3 matching with the crystallographic plane reflections of (211), (220), (222), and (433), correspondingly (ICDD PDF card # 78-0390), and the distinct signals at 36.28°, 40.67°, 41.80°, 57.73°, and 64.17° could be assigned to Mn_3O_4 corresponding to the crystallographic plane reflections of (112), (130), (131), (115), and (063), respectively (ICDD PDF card # 75-0765) [28,29]. Comparing the pattern of Mn−Co/TiO_2 nanocatalyst, it could be noticed that the diffraction peaks of both Mn_2O_3 and Mn_3O_4 were remarkably decreased in Mn−Fe/TiO_2 nanocatalyst, simultaneously, the diffraction peaks matched anatase TiO_2 were also visibly weakened. These possibly suggested the addition of cobalt into manganese oxides had better effects than iron on diminishing the crystallization of MnO_x and TiO_2 at the same time. Furthermore, there were no obvious distinct diffraction peaks of CoO_x were observed in Mn−Co/TiO_2 nanocatalysts, which indicated the addition ratios of cobalt not only enhanced the dispersion of MnO_x, but also

promoted the dispersion of CoO_x entirely on the nanocatalyst surface. A similar proposal could be obtained over Mn−Fe/TiO_2 nanocatalysts. Generally, among Mn−Ce/TiO_2, Mn−Co/TiO_2, and Mn−Fe/TiO_2 nanocatalysts, the $MnCeO_x$ loading on anatase TiO_2 performed the superior properties with smaller the nanoparticle sizes, reducing the chemical compounds crystallinities and increasing the active species distributions, which were facilitated to the SCR reactions [30]. In order to confirm the presence of nitrates in the mixtures during the plasma-catalyst process, the Energy Dispersive Spectrometer (EDS) test was introduced to qualitatively analyze the elements changes, as exhibited in Figure 5b. It was apparent that the variation of nitrogen contents on the Mn−Ce/TiO_2 sample before and after the plasma-catalyst reaction was tiny, which indicated little deposition of nitrates on the catalyst surface.

2.4.2. Reducibility Properties

In order to explore the oxidation states and the reduction potentials of the active species contained in the Mn-based bimetallic nanocatalysts, H_2-TPR analysis was performed with the reduction peaks fitted by Gaussian functions, as exhibited in Figure 6. The H_2 consumptions together with all reduction temperature values were summarized in Table 3. On account of the support of anatase TiO_2 induced no noteworthy reduction peaks in the test temperature region, all the H_2 consumption peaks displayed in Figure 6 could be ascribed to the reduction reactions of diverse active species of MnO_x, CeO_x, CoO_x, and FeO_x. For Mn-based catalysts, the typical reduction peaks were regard as following the order of $MnO_2 \rightarrow Mn_2O_3$ (Mn_3O_4) $\rightarrow$MnO [31]. For Mn−Ce/TiO_2 nanocatalyst, as shown in Figure 6a, there were five main H_2 consumption peaks appearing within the temperature range of 50~850 °C. The initial dominating reduction peak (R1) at around 261 °C was mainly caused by the reduction reaction of the high oxidation state of Mn^{4+} reducing to Mn^{3+} [32]. The subsequent asymmetrical reduction peak from 260 °C to 410 °C could be further divided into two reduction peaks (R2 and R3), according to the two processes of Mn_2O_3 reducing to Mn_3O_4 and Mn_2O_3 reducing to MnO reported in previous literatures [28,31]. The converting from Mn_2O_3 to Mn_3O_4 preferred to occur on the primal amorphous Mn_2O_3 [33], which was consistent with appearance of R2 peak. While the transformation from Mn_2O_3 to MnO was apt to happen at higher reaction temperatures [34], well coinciding with the temperature value of R3 peak. For Ce-containing sample, the typical CeO_x reduction process usually presented two separated peaks, the one of $CeO_2{}^s$ converting to $Ce_2O_3{}^s$ on the catalyst surface occurred at about 450 °C, the other one of $CeO_2{}^b$ transforming to $Ce_2O_3{}^b$ in the catalyst bulk came up at 730 °C approximately [35]. Therefore, the fourth wide reduction peak (R4) in the Mn−Ce/TiO_2 nanocatalyst was related to the reduction processes of Mn_3O_4 to MnO and $CeO_2{}^s$ to $Ce_2O_3{}^s$ simultaneously, and the fifth peak (R5) at around 717 °C was potentially associated with the $CeO_2{}^b$ reduction reaction. Among these three Mn-based bimetallic nanocatalysts, Mn−Ce/TiO_2 nanocatalyst displayed the highest low-temperature reducibility and exhibited a noticeable lack of high-temperature reduction peaks at the same time, which manifested the higher oxidation states of manganese ion (Mn^{4+} and Mn^{3+}) constituted the dominating phase [34].

Comparing with Mn−Ce/TiO_2 nanocatalyst, the H_2-TPR curve of Mn−Co/TiO_2 nanocatalyst was conspicuously different in both the reduction temperatures and the peak intensions. For Mn−Co/TiO_2 nanocatalyst, the reduction peak of MnO_2 to Mn_2O_3 shifted toward lower temperature (218 °C) and weakened significantly. Meanwhile, the reduction peaks of Mn_2O_3 to Mn_3O_4 and Mn_2O_3 to MnO moved to higher temperatures and strengthened noticeably. The two reduction processes of Mn_2O_3 presented as a whole peak centered at about 418 °C. The reduction reaction of cobalt oxides exhibited two peaks at around 327 (R2) and 517 °C (R4), which could be ascribed to the transformation of $Co^{3+} \rightarrow Co^{2+}$ and $Co^{2+} \rightarrow Co^0$, respectively [15]. However, these two reduction peaks were overlapped with the MnO_x peaks in whole or partly. For Mn−Fe/TiO_2 nanocatalyst, considering the coexistence of FeO_x and MnO_x, the joint peaks (R2 and R3) from 330 °C to 530 °C were mainly attributed to the conversion of Mn_2O_3 to Mn_3O_4 combining with the transformation of Fe_2O_3 to Fe_3O_4. According to previous report [36], the majority of Fe_2O_3 ($Fe_2O_3{}^m$) was in the form of nanoparticles, oligomeric

clusters or isolated ions locating at effortlessly reducible sites. After the $Fe_2O_3^m$ reduction reaction, the reduction of residual Fe_2O_3 ($Fe_2O_3^r$) to Fe_3O_4 accomplished at the higher temperature [37]. The remarkable strong peak (R4) at about 501 °C was ascribed to the overlapped peaks of Mn_3O_4 to MnO and Fe_3O_4 to FeO.

As exhibited in Table 3, the total H_2 consumptions of Mn−Ce/TiO_2 and Mn−Co/TiO_2 nanocatalysts were 4.86 mmol·g^{-1} and 4.43 mmol·g^{-1}, respectively, much larger than that of Mn−Fe/TiO_2 nanocatalysts. It was proposed that the peaks appearing at lower temperatures demonstrated superior catalytic activity in low temperature region [2]. While the starting reduction peak temperature of Mn−Co/TiO_2 nanocatalyst was the lowest at 218 °C, its total H_2 consumption was obvious smaller than that of Mn−Ce/TiO_2 nanocatalyst, which was regarded as a more important factor affecting the reducing capacity. Based on the H_2 consumption as a vital factor to the redox property of catalyst, it was reasonable that Mn−Ce/TiO_2 nanocatalyst presented the higher NO_x conversion with and without plasma than Mn−Co/TiO_2 and Mn−Fe/TiO_2 nanocatalysts.

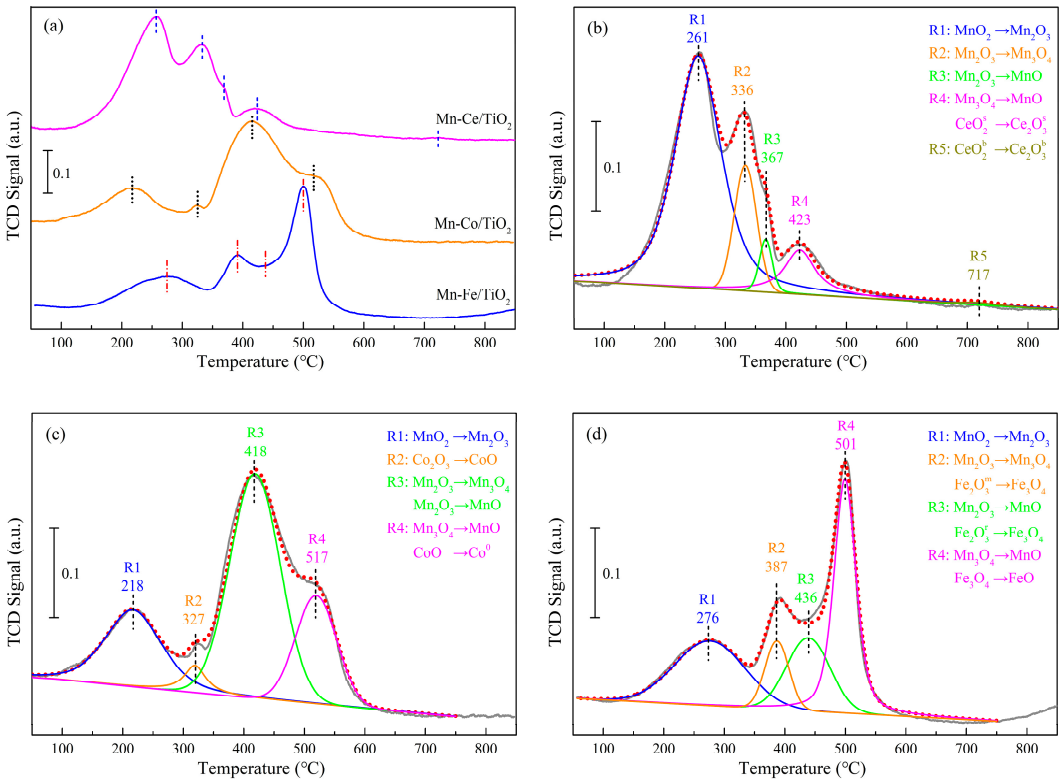

Figure 6. H_2-TPR profiles of Mn-based bimetallic nanocatalysts: (**a**) Total H_2-TPR curves; (**b**) multi-peaks Gaussian fitting for Mn−Ce/TiO_2 nanocatalyst; (**c**) multi-peaks Gaussian fitting for Mn−Co/TiO_2 nanocatalyst; and (**d**) multi-peaks Gaussian fitting for Mn−Fe/TiO_2 nanocatalyst.

Table 3. H_2-TPR quantitative analysis of Mn-based bimetallic nanocatalysts.

Samples	Temperature (°C)					H_2 Consumption (mmol·g^{-1})					
	R 1	R 2	R 3	R 4	R 5	R 1	R 2	R 3	R 4	R 5	Total
Mn−Ce/TiO_2	261	336	367	423	717	2.52	1.24	0.36	0.67	0.07	4.86
Mn−Co/TiO_2	218	327	418	517	–	1.14	0.21	2.12	0.96	–	4.43
Mn−Fe/TiO_2	276	387	436	501	–	0.83	0.41	0.54	1.59	–	3.37

2.4.3. Ammonia Adsorption Properties

Besides the redox property, the acid capacity on the catalyst surface was another crucial factor influencing the catalytic performance in SCR reactions [14,38]. NH_3-TPD and NO-TPD tests were introduced in order to establish the connection between the surface acidities and the SCR activities for

the Mn-based bimetallic nanocatalysts. The test results were analyzed and compared in Figure 7 and Table 4, respectively. The NH_3-TPD curves for these three typical Mn-based bimetallic nanocatalysts were attributed to four desorption peaks of chemisorbed NH_3 within the temperature range of 150~750 °C. It was obvious that the first weak NH_3 desorption peak (P1) of Mn−Fe/TiO_2 nanocatalyst appeared at about 209 °C ascribed to the NH_3 desorption from the weak acid sites, which was deemed too weak to be stable bound NH_3 in the gas mix during the SCR reactions [14]. The second and the third successive desorption peaks (P2 and P3) located from 398 °C to 585 °C indicated the distribution of medium strong acid sites. Additionally, the final and relatively stronger peak (P4) at 649 approximately were attributed to strong acid sites, which could be regard as plenty of Lewis acid sites generated on the nanocatalyst surface with adsorbing a large amount of strongly bound ammonia [39]. For Mn−Co/TiO_2 nanocatalyst, the NH_3 desorption result demonstrated superior acidity capacity at medium and high temperatures, but an undesirable temperature shift towards higher temperature regions appeared at the same time. The desorption peak temperature value of weak acid sites (P1), medium strong acid sites (P2 and P3), and strong acid sites (P4) reached 276 °C, 402 °C, 587 °C, and 653 °C, respectively, which signified that it is more difficult for the chemisorbed NH_3 to desorb from the acid sites and participate in SCR reactions [40]. Compared with the NH_3-TPD curve of Mn−Co/TiO_2 nanocatalyst, the four desorption peaks of Mn−Ce/TiO_2 nanocatalyst shifted towards lower temperatures slightly and became much stronger. The enrichments of the weak acid sites, the medium strong acid sites and the strong acid sites were all positive to ammonia adsorption, which could undoubtedly form more abundant Brønsted acid sites and Lewis acid sites promoting NH_3 adsorption on the nanocatalyst surface [41,42]. This change was regard as an important reason for the outstanding catalytic performance of Mn−Ce/TiO_2 nanocatalyst with and without plasma.

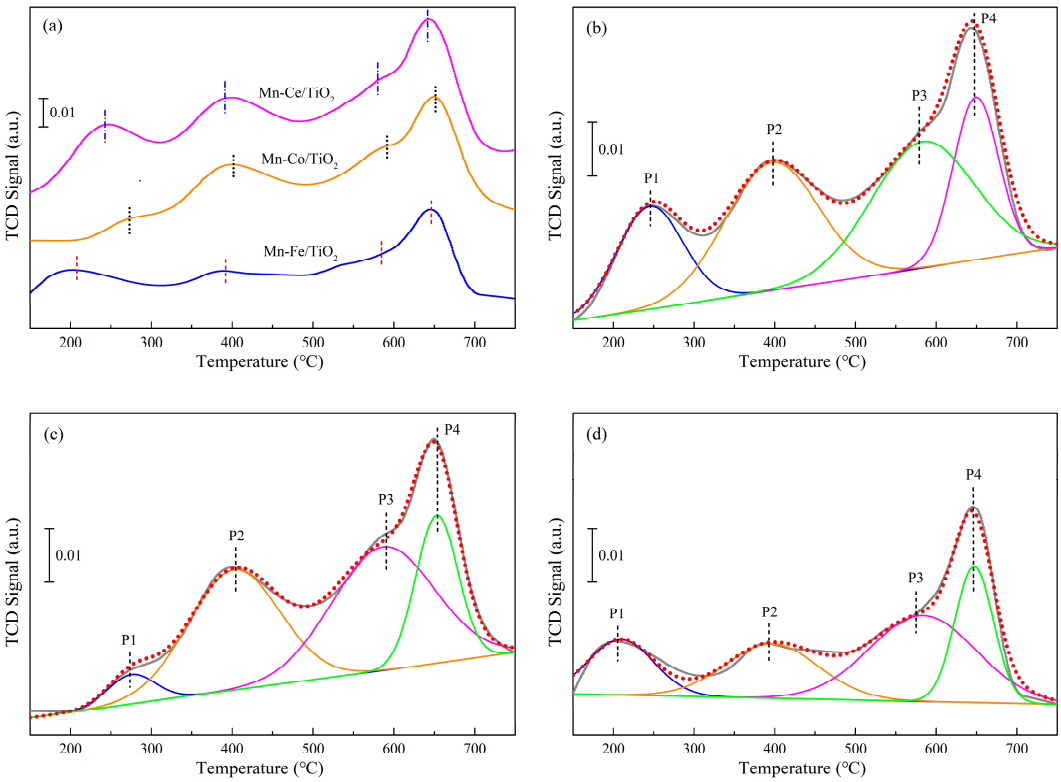

Figure 7. NH_3-TPD profiles of Mn-based bimetallic nanocatalysts: (**a**) Total NH_3-TPD curves; (**b**) multi-peaks Gaussian fitting for Mn−Ce/TiO_2 nanocatalyst; (**c**) multi-peaks Gaussian fitting for Mn−Co/TiO_2 nanocatalyst; (**d**) multi-peaks Gaussian fitting for Mn−Fe/TiO_2 nanocatalyst.

Table 4. Quantitative analysis of NH_3-TPD profiles.

Samples	Temperature (°C)				NH_3 Composition (mmol·g^{-1})				
	Peak 1	Peak 2	Peak 3	Peak 4	Peak 1	Peak 2	Peak 3	Peak 4	Total
Mn−Ce/TiO_2	245	396	583	647	0.27	0.52	0.58	0.39	1.76
Mn−Co/TiO_2	276	402	587	653	0.11	0.49	0.52	0.32	1.44
Mn−Fe/TiO_2	209	398	585	649	0.14	0.24	0.39	0.20	0.97

In order to exactly confirm the total acid capacity, the quantitative analysis of the desorption peaks of Mn−Ce/TiO_2, Mn−Co/TiO_2 and Mn−Fe/TiO_2 nanocatalyst was performed and summarized in Table 4. Among these three nanocatalysts, the total NH_3 desorption of Mn−Ce/TiO_2 sample achieved the maximum value of 1.76 mmol·g^{-1}, which further verified the better promotion effects of $MnCeO_x$ on the surface acidity than that of $MnCoO_x$ and $MnFeO_x$. It was noteworthy that, although Mn−Fe/TiO_2 nanocatalyst exhibited the weak acid sites at the lowest temperature, the acid capacity of its weak acid sites was only 0.14 mmol·g^{-1} too small to satisfy the NH_3 adsorption requirements during SCR recations. Therefore, Mn−Ce/TiO_2 nanocatalyst with NH_3 desorption of 0.27 mmol·g^{-1} at around 245 °C was qualified for the best acidity properties at the low temperature. However, it had been revealed that NH_3 could block NO adsorption and activation onto the metal active sites on the catalyst surface via the undesired electronic contact between the adsorbed NH_3 and the metal sites [43]. As a result, NH_3 presented inhibiting effects on SCR reactions at low temperature. Hence, the acidity properties on the surface of the Mn-based bimetallic nanocatalysts were closely related to the redox performance. It was required to achieve an adequate equilibrium between the oxidation states of active species and the acidity properties of active metal compounds in order to develop the optimal catalyst.

2.4.4. Oxidation States of Active Species

The elemental valence states and the atomic concentrations on the surface of Mn-based bimetallic nanocatalysts were explored by XPS analysis for the purpose of a better insight into the metal oxidation states and the surface compositions. The XPS spectra of Mn 2*p*, O 1*s*, Ti 2*p*, Fe 2*p*, Co 2*p*, and Ce 3*d* in the nanocatalysts were exhibited in Figure 8. The valence state of every element was determined numerically according to Gaussian fitting, respectively. The specific binding energy and the individual element concentration in various valence states were summarized in Table 5. Figure 8a displayed the XPS spectrum for Ti 2*p* of catalyst support, which comprised two peaks of Ti $2p_{1/2}$ locating at about 464.3 eV and Ti $2p_{3/2}$ situating at around 458.7 eV, respectively [44]. Comparing the three XPS spectrum of Ti, it could be easily found that, although the Mn-based bimetallic nanocatalysts were doped with different active elements of iron, cobalt, and manganese, no significant changes were observed in the Ti peaks. The +4 valence state of titanium on the catalyst surface was stabilized and dominating in Mn−Fe/TiO_2, Mn−Co/TiO_2, and Mn−Ce/TiO_2 nanocatalysts.

The XPS spectra of Mn 2*p* in these three typical Mn-based bimetallic nanocatalysts consisted of two characteristic peaks, assigned to Mn $2p_{1/2}$ peak at around 653 eV and Mn $2p_{3/2}$ peak at about 642 eV [45], as shown in Figure 8b. The asymmetrical Mn $2p_{3/2}$ peak further verified the complicated manganese species in divers valence states coexisting in the nanocatalysts. The curve of Mn $2p_{3/2}$ peak could be split into three peaks via multi-peaks gaussian fitting, the first peak at around 641.2 ± 0.3 eV was assigned to Mn^{2+}, the second one at 642.6 ± 0.2 eV associated with Mn^{3+}, and the third one at 644.1 ± 0.5 eV consistent with Mn^{4+}, respectively [46]. The complex MnO_x including three valence states were apparently difficult to distinguish with the binding energy difference no more than 3.7 eV. In order to make an accurate identification of the atomic composition and Mn^{n+} concentration on the nanocatalyst surface, a quantitative analysis was introduced based on the area covered under each separated peak, as listed in Table 4. According to previous studies [28,33,47], NO_x conversion over pure MnO_x could been ranked as MnO_2 > Mn_2O_3 > Mn_3O_4. Hence, the improved concentration of MnO_2 on the nanocatalyst surface was advantageous to SCR reactions [48]. Among the three Mn-based

bimetallic nanocatalysts, the major amount of manganese primarily presenting +4 valence state on the catalyst surface dispersedly, as shown in Table 4. While Mn−Ce/TiO_2 sample presented the highest atomic composition of Mn^{4+}/Mn^{n+} (56.5%), which was much larger than 46.8% and 40.2% in Mn−Co/TiO_2 and Mn−Fe/TiO_2 nanocatalysts, respectively. It was regard as the reason for the higher catalytic activity of Mn−Ce/TiO_2 nanocatalyst, as exhibited in the above results.

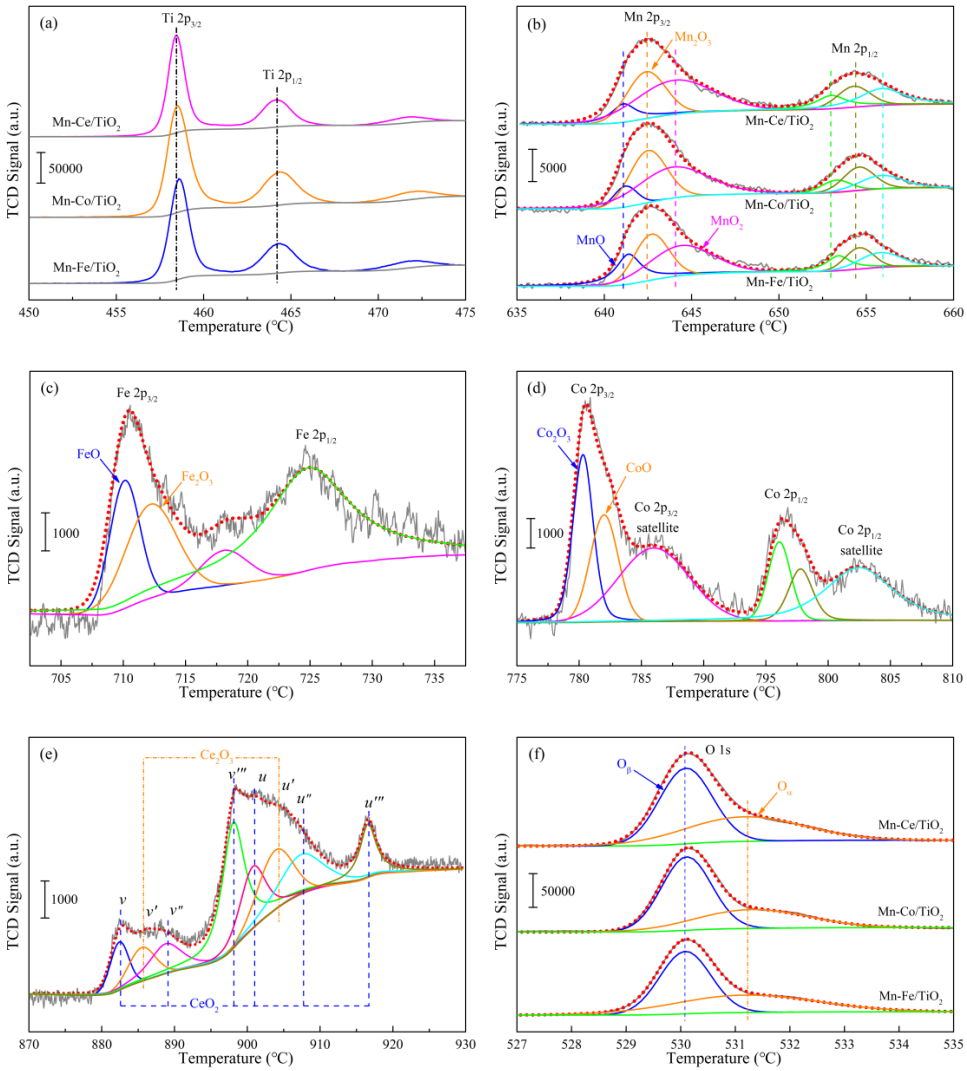

Figure 8. XPS analysis of Mn-based bimetallic nanocatsalysts: (**a**) XPS spectra for Ti 2*p*; (**b**) XPS spectra for Mn 2*p*; (**c**) XPS spectra for Fe 2*p*; (**d**) XPS spectra for Co 2*p*; (**e**) XPS spectra for Ce 3*d*; and (**f**) XPS spectra for O 1*s*.

Table 5. Surface atomic compositions of the catalysts determined by XPS.

Samples	Binding Energy (eV)/Atomic Composition (%)										
	Mn			Fe		Co		Ce		O	
	Mn^{2+}	Mn^{3+}	Mn^{4+}	Fe^{2+}	Fe^{3+}	Co^{2+}	Co^{3+}	Ce^{3+}	Ce^{4+}	O_α	O_β
Mn−Ce/TiO_2	640.9/ 9.3	642.4/ 34.2	644.0/ 56.5	-/-	-/-	-/-	-/-	885.6/ 40.4	882.4/ 59.6	531.2/ 40.4	530.2/ 59.6
Mn−Co/TiO_2	641.2/ 13.8	642.6/ 39.4	644.1/ 46.8	-/-	-/-	779.6 39.3	782.1/ 60.7	-/-	-/-	531.4/ 33.7	530.3/ 66.3
Mn−Fe/TiO_2	641.4/ 21.3	642.8/ 38.5	644.6/ 40.2	709.6/ 43.4	711.7/ 56.6	-/-	-/-	-/-	-/-	531.6/ 28.2	530.3/ 71.8

For Mn−Fe/TiO_2 nanocatalyst, the Fe 2p XPS spectra was was presented in Figure 8c with two individual peaks attributed to Fe $2p_{3/2}$ at about 710 eV, Fe $2p_{1/2}$ at around 724 eV and a satellite peak of Fe^{3+} in Fe_2O_3 exhibited at 718.3 eV [49]. The broad peak of Fe $2p_{3/2}$ was composed of two overlapped peaks, the one ascribed to Fe^{2+} locating at around 709.6 eV and the other one attributed to Fe^{3+} seated at about 711.6 eV. These two peaks confirmed the co-occurrence of iron in +2 and +3 valence states on Mn−Fe/TiO_2 nanocatalyst surface, as quantified in Table 5. The promotion effect of iron on Mn-based bimetallic nanocatalysts was ascribed to the interaction happening in the redox circulation: Fe^{3+} + Mn^{3+} ↔ Fe^{2+} + Mn^{4+} [50]. For Mn−Co/TiO_2 nanocatalyst, there were two main peaks in the Co 2*p* spectrum ascribed to Co $2p_{3/2}$ at about 780.6 eV and Co $2p_{1/2}$ at around 796.5 eV. Each of these two peaks was accompanied by an adjacent satellite peak at 786.8 eV and 803.1 eV correspondingly, as depicted in Figure 8d. The two broader and gentler satellite structures at the relatively higher binding energy region were caused by the metal-to-ligand charge transfer, also known as the shakeup process of cobalt in its high spin state. While this process can only be observed with the high spin state of Co^{2+} ion, but cannot be observed with the diamagnetic low-spin Co^{3+} ion [51]. The XPS spectra of Co $2p_{3/2}$ scope could be further divided into Co^{3+} spectrum at binding energy of 780.0 eV and Co^{2+} spectrum at 781.6 eV. This test result showed the ions of Co^{2+} and Co^{3+} were co-existed on Mn−Co/TiO_2 nanocatalyst surface and the Co^{3+} exhibited a comparatively higher atomic composition of 60.7%. The Co^{3+} species existed in a relatively high valence state and gave rise to more anionic defects, generating abundant surface oxygen to enhance the process of adsorption and oxidation during SCR reactions [52]. For Mn−Ce/TiO_2 nanocatalyst, the Ce 3*d* spectra result was depicted in Figure 8e. The Ce 3*d* pattern was composed of u and v multi-peaks matching to the spin orbit split $3d_{5/2}$ and $3d_{3/2}$ core holes [53]. According to the binding energies of different peaks, the Ce 3*d* spectra could be elaborately separated into eight peaks, labeled as u, u', u'', u''' and v, v', v'', v''', respectively [54]. The u' and v' peaks were matched with the $3d^{10}4f^1$ electronic state of Ce^{3+}, and the u, u'', u''', v, v'', and v''' peaks were ascribed to the $3d^{10}4f^0$ electronic state of Ce^{4+} [55]. These distinctive peaks verified the coexistence of of Ce^{3+} and Ce^{4+} species on Mn−Co/TiO_2 nanocatalyst surface. The Ce^{3+} species were important incentives for the formation of unsaturated chemical bonds and the generation of electric charge balance. [56]. In the active compounds of manganese and cerium, the negative charge transferred from Mn^{2+} or Mn^{3+} to Ce^{4+} strengthening the interaction between manganese and cerium [1,2]. The oxygen circle of storing and releasing was easier for the Mn−Ce/TiO_2 nanocatalyst with the redox couple of Ce^{3+}/Ce^{4+} to form more surface oxygen vacancies that were advantageous to oxygen adsorption and chemisorbed oxygen generation [57].

The O 1*s* spectra for Mn-based bimetallic nanocatalysts were displayed in Figure 8f. On the base of curve-fitting results, the O 1*s* spectra was divided into two peaks: The O_α peak ascribed to chemisorbed oxygen centered at binding energy of 531.2 ~ 531.6 eV, the O_β peak attributed to lattice oxygen appeared at binding energy of 530.2 ~ 530.3 eV. Compared with the O 1*s* spectra of nanocatalysts, it could be found that the binding energies of O_α shifted to lower values from 531.6 eV in Mn−Fe/TiO_2 to 531.4 eV in Mn−Co/TiO_2 and to 531.2 eV in Mn−Ce/TiO_2, and similar variation tendency occurred on the binding energies of O_β. Meanwhile, as shown in Table 4, the surface atomic composition of chemisorbed oxygen over Mn−Ce/TiO_2 nanocatalyst reached the maximum 40.4%, much higher than 33.7% on Mn−Co/TiO_2 and 28.2% on Mn−Fe/TiO_2 samples. The chemisorbed oxygen was the most energetic oxygen species due to its high mobility [58]. Therefore, these surface atomic composition of Mn−Ce/TiO_2 nanocatalyst were regard as another reason for its superior catalytic performance with and without plasma.

2.5. Reaction Mechanism Analysis

According to the catalytic performance of NO_x conversion over Mn-based bimetallic nanocatalysts with and without plasma and the physicochemical properties of these nanocatalysts presented above, the complex bimetallic oxides of $MnFeO_x$, $MnCoO_x$, and $MnCeO_x$ affected the hybrid catalyst-plasma catalytic process obviously with the different redox characteristics of active chemisorbed sites. All the

three bimetallic nanocatalysts enhanced the catalytic ability of manganese species by increasing the ratio of Mn^{4+}/Mn^{n+}, generating more lattice oxygen and plenty of oxygen vacancy on the catalyst surface [2]. In the catalyst-plasma hybrid catalytic system, the plasma derivatives reformed the chemical compositions of the gas mix and modified the electronic states on the nanocatalyst surface. For $Mn-Fe/TiO_2$, $Mn-Co/TiO_2$ and $Mn-Ce/TiO_2$ nanocatalysts, a dynamic equilibrium was sustained on their surfaces with the electron transfer between Mn and Fe (Co or Ce) ions during the catalytic oxidation process, which could be expressed as $Fe^{3+} + Mn^{3+} \leftrightarrow Fe^{2+} + Mn^{4+}$, $Co^{3+} + Mn^{3+} \leftrightarrow Co^{2+} + Mn^{4+}$, $Ce^{3+} + Mn^{3+} \leftrightarrow Ce^{2+} + Mn^{4+}$ and $Ce^{4+} + Mn^{3+} \leftrightarrow Ce^{3+} + Mn^{4+}$, respectively.

Besides originally partial NO oxidation into NO_2 over the lattice oxygen of MnO_x, FeO_x, CoO_x and CeO_x, more NO was oxidized to NO_2 via the reaction (4) and (5) under the energetic particles. The valence state part of manganese cations increased, which was caused by the electron transition from Mn^{3+} to Mn^{4+} via lattice oxygen [59]. Mn^{4+} was more desirable for the oxidation of NO to NO_2 over Mn-based catalysts [16] and it was reduced to Mn^{3+} during the SCR reactions [58]. Under the plasma derived species, such as O_3 or O radicals, the Mn^{3+} could be fast re-oxidation into Mn^{4+}, thus accelerating the catalytic oxidation process and the fast SCR reaction. Furthermore, the concentration of chemisorbed oxygen on the nanocatalyst surface was also improved in the catalyst-plasma hybrid catalytic system. More surface oxygen species could form via the direct interaction of MnO_x, FeO_x, CoO_x, and CeO_x with plasma excited oxygen species. Considering the inhibiting effect of NO on O_3 formation, the surface oxygen species were more likely to generate from O radicals. The adsorbed oxygen reacted with NO to form NO_2 according to the following reaction steps (9)~(11):

$$O + M \rightarrow M - O_{ads} \tag{9}$$

$$NO + M - O_{ads} \rightarrow M - O - NO_{ads} \tag{10}$$

$$M - O - NO_{ads} \rightarrow M + NO_2 \tag{11}$$

where M represented the active sites on the nanocatalyst surface, O_{ads} and NO_{ads} represented adsorbed NO and oxygen on the nanocatalyst surface, respectively. During this process, the NO_{ads} liberated electron to Mn^{4+} and the O_{ads} trapped electron from Fe^{2+} or Co^{2+} or Ce^{3+}, respectively, which transform into absorbed NO^+ and O^-. Then formed NO^+ further reacted with O^- to generate NO_2. Simultaneously, a part of NO was oxidized to NO_2 directly by the active oxygen produced from O_2 activation on the surface oxygen vacancies. The possible catalyst-plasma hybrid catalytic process of SCR reaction over Mn-based bimetallic nanocatalysts was exhibited in Figure 9.

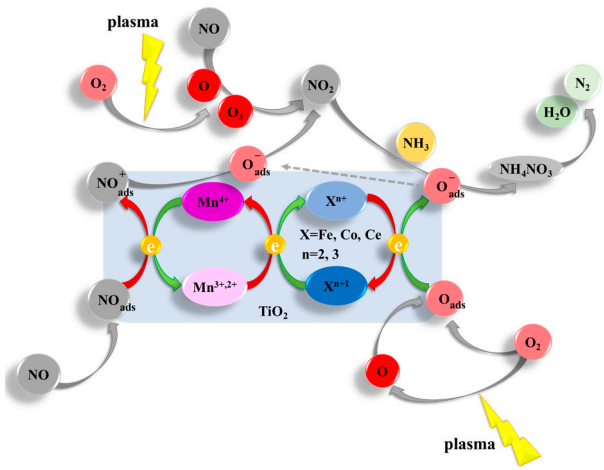

Figure 9. The possible catalyst-plasma hybrid catalytic process of SCR reaction over Mn-based bimetallic nanocatalysts.

3. Materials and Methods

3.1. Catalysts Preparation

The three typical Mn-based bimetallic nanocatalysts were prepared by hydrothermal method. $Mn(NO_3)_2$ (analytical pure 50%, Sinopharm, Shanghai, China), $Fe(NO_3)_3 \cdot 9H_2O$ (analytical pure 99.9%, Sinopharm, Shanghai, China), $Co(CH_3COO)_2 \cdot 4H_2O$ (analytical pure 99.9%, Kermel, Tianjin, China), and $Ce(NO_3)_3 \cdot 6H_2O$ (analytical pure 99.9%, Nanjing-reagent, Nanjing, China) were introduced as the precursors of MnO_x, FeO_x, CoO_x, and CeO_x, respectively. The tetrabutyl titanate was used as the precursors of TiO_2 for supporting the active metallic oxides. $Mn(NO_3)_2$ was added into deionized water at room temperature and then $Fe(NO_3)_3 \cdot 9H_2O$ was dissolved in the solution. Amount of glycol was added into the above mixture with magnetic stirring continuously. A Teflon-lined stainless steel autoclave was introduced to heat the homogeneous solution at 180 °C for 8 h. After the autoclave cooling down to the ambient temperature, tetrabutyl titanate was added into this solution and aged in the autoclave again at 180°C for 3 h. The mixture was collected by reduplicative centrifugation and wash. Finally, the precipitate was dried at 150 °C for 12 h and calcined in air at 500 °C for 4 h. The produced Mn-based bimetallic nanocatalysts were triturated and filtered with 60−80 mesh for activity tests and characterization analysis. The nanocatalyst was denoted as $Mn-Fe/TiO_2$ with the molar ratios of Mn:Fe:Ti = 2:1:7. The $Mn-Co/TiO_2$ and $Mn-Ce/TiO_2$ nanocatalysts were prepared under the same process with $Co(CH_3COO)_2 \cdot 4H_2O$ and $Ce(NO_3)_3 \cdot 6H_2O$ replacing $Fe(NO_3)_3 \cdot 9H_2O$, respectively.

3.2. Catalysts Characterization

The Maxon Tristar II 3020 micropore-size analyzer (Maxon, Chicago, IL, USA) was used for testing N_2 adsorption isotherms of the prepared nanocatalysts at -196 °C. The surface areas and the pore-size distributions of the nanocatalysts were measured after the nanocatalysts degassing in vacuum at 350 °C for 10 h. BET plot linear portion was used to determine the nanocatalysts specific surface areas, and the desorption branch with Barrett–Joyner–Halenda (BJH) formula was introduced to calculate the pore-size distributions. The XRD data was captured by a Bruker D8 advance analyzer (Bruker, Frankfurt, Germany) with Mo K_α radiation, diffraction intensity from 10° to 90°, point counting time of 1s and point counting step of 0.02°. The element phases contained in the nanocatalys were distinguished by comparing characteristic peaks presented in the XRD patterns with the International Center for Diffraction Data (ICDD). The advanced microstructural image data and the surface element contents of the nanocatalysts were achieved by a high resolution transmission electron microscope JEOL JEM-2010 combined with EDS ((Japan electronics corporation, Tokyo, Japan). H_2-TPR and NH_3-TPD tests were performed with a Micromeritics Autochem II 2920 chemical adsorption instrument (Micromeritics, Houston, TX, USA). During H_2-TPR experiment, nanocatalysts were pretreatment in He at 400 °C for 1 h, and then cooled to environment temperature in H_2 and He gas mixture at 30 mL/min. The test temperature range of H_2 consumptions was from 50 °C to 850 °C with the heating rate of 10 °C/min. The operating process of NH_3-TPD test was similar to that of H_2-TPR test with NH_3 replacing H_2. XPS analysis was performed on a Thermo ESCALAB 250XI (Thermo Fisher, Boston, MA, USA) with pass energy 46.95 eV, Al K_α radiation 1486.6 eV, X-ray source 150 W and binding energy precision ± 0.3 eV. The C 1*s* line at 284.6 eV was measured as a reference.

3.3. Catalytic Performance Tests

The catalytic performance of Mn-based bimetallic nanocatalysts was explored in a catalyst-plasma hybrid system as shown in Figure 10. The dielectric barrier discharge (DBD) plasma reactor was comprised of two electrodes and a quartz tube. The high voltage electrode was a stainless-steel rod with diameter of 3 mm, installed inside the quartz tube coaxially. The ground electrode was a copper wire mesh wrapped outside the quartz tube tightly. The discharge energy was produced by an AC power transverter with a digital controller of voltage, electricity, and frequency. The quartz tube was in the height of 800 mm, outer diameter of 12 mm and thicknesses of 0.8 mm. 5 mL of nanocatalyst

was filled in the discharge zone of plasma reactor. A resistance furnace was introduced to maintain the desired reaction temperature located upstream plasma reactor, connected to the temperature controller. The concentration of gas mixture was measured by German MRU MGA-5 analyzer (MRU, Berlin, Germany) joint with an external special detector for N_2O and NH_3. An Infrared Thermometer (HCJYET, HT-8872, Hongcheng, Shanghai, China) was introduced to detect the specific temperature of discharge area during the plasma process. During plasma-catalyst catalytic activity experiment, the inlet mixed gas included 300 ppm NO, 300 ppm NH_3, 8% O_2, ~0.1% H_2O and N_2 as balance gas. The gas hourly space velocity (GHSV) was about 20 000 h^{-1}. The NO_x conversion rate was calculated according to Equation (12), where $[NO_x] = [NO] + [NO_2]$. The N_2 selectivity was calculated by the concentrations of N_2O and NO_x, as shown in Equation (13). Each experiment was repeated three times to assure the results accuracy. The discharge energy density was defined as discharge power divided by the inlet gas flow rate [9], which was calculated using Equation (14) [60], where E ($W{\cdot}h/m^3$) was energy density, P (W) was discharge power, and Q (m^3/h) was the gas flow rate. More basic data relating to the discharge energy was listed in Table 1.

$$NO_x \text{ conversion rate} = \left(\frac{[NO_x]_{in} - [NO_x]_{out}}{[NO_x]_{in}}\right) \times 100\% \tag{12}$$

$$N_2 \text{ selectivity} = 1 - \frac{2[N_2O]_{out}}{[NO_x]_{in} - [NO_x]_{out}} \times 100\% \tag{13}$$

$$E\ (W{\cdot}h/m^3) = \frac{P\ (W)}{Q\ (m^3/h)} \tag{14}$$

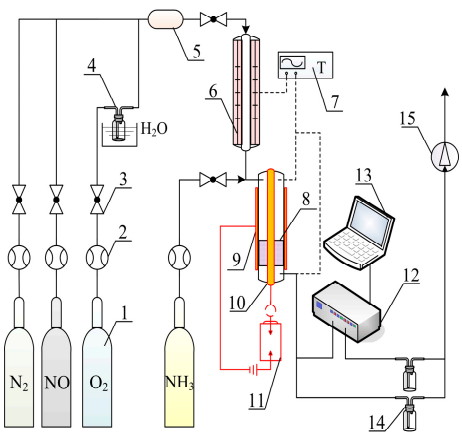

Figure 10. The schematic diagram about the catalyst-plasma hybrid system. 1, standard gas; 2, mass flowmeter; 3, shutdown valve; 4, water carrier; 5, gas mixer; 6, resistance furnace; 7, temperature controller; 8, nanocatalysts; 9, ground electrode; 10, high voltage electrode; 11, AC power transverter; 12, flue gas analyzer; 13, record system; 14, gas washing bottle; and 15, induced draft fan.

4. Conclusions

The Mn-based bimetallic nanocatalysts of $Mn{-}Fe/TiO_2$, $Mn{-}Co/TiO_2$, $Mn{-}Ce/TiO_2$, synthesized by hydrothermal method, presented obvious synergistic effects on NO_x catalytic conversion via the plasma-catalyst hybrid catalytic process. In the catalytic process with catalyst alone, the NO_x conversions of all tested catalysts were lower than 20% at ambient temperature. While in the plasma-catalyst hybrid catalytic process, the catalytic activities for NO_x elimination improved significantly with discharge energy enlarging. The maximum NO_x conversion of about 99.5% achieved on $Mn{-}Ce/TiO_2$ with discharge energy of 15 $W{\cdot}h/m^3$ at ambient temperature. The reaction temperature had an inhibiting effect on plasma-catalyst hybrid catalysis.

Among these three Mn-based bimetallic nanocatalysts, Mn−Ce/TiO_2 displayed the optimal catalytic property with higher catalytic activity and superior selectivity in the plasma-catalyst hybrid catalytic process. Furthermore, based on the multiple characterizations performed on the Mn-based bimetallic nanocatalysts, it could be confirmed that the catalytic property of plasma-catalyst hybrid catalytic process was highly dependent on the phase composition of the catalyst. Mn−Ce/TiO_2 nanocatalyst presented the optimal structure characteristic among all tested samples, with the largest surface area, the increased active components distributions, the reduced crystallinity and the minished particle sizes. In the meantime, the ratios of $Mn^{4+}/(Mn^{2+} + Mn^{3+} + Mn^{4+})$ in the Mn−Ce/TiO_2 sample was the highest, which was beneficial to plasma-catalyst hybrid catalysis. Generally, it was believed that the plasma-catalyst hybrid catalytic process with the Mn-based bimetallic nanocatalyst was an effective approach for high-efficiency catalytic conversion of NO_x, especially at ambient temperature.

Author Contributions: Conceptualization, Y.G.; Funding acquisition, Y.G., T.L., W.Z.; Methodology, Y.G., T.L.; Project administration, Y.G.; Writing–original draft, Y.G.; Writing–review & editing, H.L. and W.Z.; Data curation, Y.G., W.J., W.F., H.J.

Funding: This work was supported by National Natural Science Foundation of China (Project No. 51708336), Shandong Provincial Natural Science Foundation (ZR2016EEB28), Shandong Provincial Science and Technology Development Plan (2011GSF11716), Shandong Jianzhu university open experimental project (2018yzkf023, 2018wzkf013,), and the Shandong electric power engineering consulting institute science and technology project (37-K2014-33).

Conflicts of Interest: The authors declare no conflict of interest.

References

1. Wang, B.; Chi, C.; Xu, M.; Wang, C.; Meng, D. Plasma-catalytic removal of toluene over CeO_2-MnOx catalysts in an atmosphere dielectric barrier discharge. *Chem. Eng. J.* **2017**, *322*, 679–692. [CrossRef]
2. France, L.J.; Yang, Q.; Li, W.; Chen, Z.; Guang, J.; Guo, D.; Wang, L.; Li, X. Ceria modified FeMnOx—Enhanced performance and sulphur resistance for low-temperature SCR of NOx. *Appl. Catal. B Environ.* **2017**, *206*, 203–215. [CrossRef]
3. Gao, Y.; Luan, T.; Lu, T.; Cheng, K.; Xu, H. Performance of V_2O_5-WO_3-MoO_3/TiO_2 catalyst for selective catalytic reduction of NOx by NH_3. *Chin. J. Chem. Eng.* **2013**, *21*, 1–7. [CrossRef]
4. Wang, T.; Liu, H.; Zhang, X.; Liu, J.; Zhang, Y.; Guo, Y.; Sun, B. Catalytic conversion of NO assisted by plasma over Mn-Ce/ZSM5-multi-walled carbon nanotubes composites: Investigation of acidity, activity and stability of catalyst in the synergic system. *Appl. Surf. Sci.* **2018**, *457*, 187–199. [CrossRef]
5. Zhang, R.; Yang, W.; Luo, N.; Li, P.; Lei, Z.; Chen, B. Low-temperature NH_3-SCR of NO by lanthanum manganite perovskites: Effect of A-/B-site substitution and TiO_2/CeO_2 support. *Appl. Catal. B Environ.* **2014**, *146*, 94–104. [CrossRef]
6. Gao, Y.; Luan, T.; Zhang, M.; Zhang, W.; Feng, W. Structure–Activity Relationship Study of Mn/Fe Ratio Effects on Mn−Fe−Ce−Ox/γ-Al_2O_3 Nanocatalyst for NO Oxidation and Fast SCR Reaction. *Catalysts* **2018**, *8*, 642. [CrossRef]
7. Miessner, H.; Francke, K.P.; Rudolph, R.; Hammer, T. NOx removal in excess oxygen by plasma-enhanced selective catalytic reduction. *Catal. Today* **2002**, *75*, 325–330. [CrossRef]
8. Kim, H.-H.; Teramoto, Y.; Ogata, A.; Takagi, H.; Nanba, T. Plasma Catalysis for Environmental Treatment and Energy Applications. *Plasma Chem. Plasma Process.* **2016**, *36*, 45–72. [CrossRef]
9. Penetrante, B.M.; Brusasco, R.M.; Merritt, B.T.; Pitz, W.J.; Vogtlin, G.E.; Kung, M.C.; Kung, H.H.; Wan, C.Z.; Voss, K.E. Plasma-Assisted Catalytic Reduction of NOx. In Proceedings of the International Fall Fuels and Lubricants Meeting and Exposition, San Francisco, CA, USA, 19–22 October 1998. [CrossRef]
10. Patil, B.S.; Cherkasov, N.; Lang, J.; Ibhadon, A.O.; Hessel, V.; Wang, Q. Low temperature plasma-catalytic NOx synthesis in a packed DBD reactor: Effect of support materials and supported active metal oxides. *Appl. Catal. B Environ.* **2016**, *194*, 123–133. [CrossRef]
11. Hammer, T.; Kishimoto, T.; Miessner, H.; Rudolph, R. Plasma Enhanced Selective Catalytic Reduction: Kinetics of NOx-Removal and Byproduct Formation. In Proceedings of the International Fuels & Lubricants Meeting & Exposition, Dearborn, MI, USA, 25 October 1999; Volume 1, pp. 3632–3641.

12. McAdams, R.; Beech, P.; Shawcross, J.T. Low Temperature Plasma Assisted Catalytic Reduction of NOx in Simulated Marine Diesel Exhaust. *Plasma Chem. Plasma Process.* **2008**, *28*, 159–171. [CrossRef]
13. Oda, T.; Kato, T.; Takahashi, T.; Shimizu, K. Nitric oxide decomposition in air by using non-thermal plasma processing—With additives and catalyst. *J. Electrost.* **1997**, *42*, 151–157. [CrossRef]
14. Zhang, C.; Chen, T.; Liu, H.; Chen, D.; Xu, B.; Qing, C. Low temperature SCR reaction over Nano-Structured Fe-Mn Oxides: Characterization, performance, and kinetic study. *Appl. Surf. Sci.* **2018**, *457*, 1116–1125. [CrossRef]
15. Qiu, L.; Pang, D.; Zhang, C.; Meng, J.; Zhu, R.; Ouyang, F. In situ IR studies of Co and Ce doped Mn/TiO_2 catalyst for low-temperature selective catalytic reduction of NO with NH_3. *Appl. Surf. Sci.* **2015**, *357*, 189–196. [CrossRef]
16. You, X.; Sheng, Z.; Yu, D.; Yang, L.; Xiao, X.; Wang, S. Influence of Mn/Ce ratio on the physicochemical properties and catalytic performance of graphene supported MnOx-CeO_2 oxides for NH_3-SCR at low temperature. *Appl. Surf. Sci.* **2017**, *423*, 845–854. [CrossRef]
17. Chen, Y.; Wang, J.; Yan, Z.; Liu, L.; Zhang, Z.; Wang, X. Promoting effect of Nd on the reduction of NO with NH_3 over CeO_2 supported by activated semi-coke: An in situ DRIFTS study. *Catal. Sci. Technol.* **2015**, *5*, 2251–2259. [CrossRef]
18. Liu, Z.; Zhu, J.; Li, J.; Ma, L.; Woo, S.I. Novel Mn–Ce–Ti Mixed-Oxide Catalyst for the Selective Catalytic Reduction of NOx with NH_3. *ACS Appl. Mater. Interfaces* **2014**, *6*, 14500–14508. [CrossRef] [PubMed]
19. Wang, T.; Zhang, X.; Liu, J.; Liu, H.; Wang, Y.; Sun, B. Effects of temperature on NOx removal with Mn-Cu/ZSM5 catalysts assisted by plasma. *Appl. Therm. Eng.* **2018**, *130*, 1224–1232. [CrossRef]
20. Penetrante, B.M.; Bardsley, J.N.; Hsiao, M.C. Kinetic Analysis of Non-Thermal Plasmas Used for Pollution Control. *Jpn. J. Appl. Phys.* **1997**, *36*, 5007. [CrossRef]
21. Heck, R.M. Catalytic abatement of nitrogen oxides–stationary applications. *Catal. Today* **1999**, *53*, 519–523. [CrossRef]
22. Kim, H.H.; Takashima, K.; Katsura, S.; Mizuno, A. Low-temperature NOx reduction processes using combined systems of pulsed corona discharge and catalysts. *J. Phys. D Appl. Phys.* **2001**, *34*, 604. [CrossRef]
23. Niu, J.; Yang, X.; Zhu, A.; Shi, L.; Sun, Q.; Xu, Y.; Shi, C. Plasma-assisted selective catalytic reduction of NOx by C_2H_2 over Co-HZSM-5 catalyst. *Catal. Commun.* **2006**, *7*, 297–301. [CrossRef]
24. Liu, Z.; Yi, Y.; Zhang, S.; Zhu, T.; Zhu, J.; Wang, J. Selective catalytic reduction of NOx with NH_3 over Mn-Ce mixed oxide catalyst at low temperatures. *Catal. Today* **2013**, *216*, 76–81. [CrossRef]
25. Li, X.; Zhang, S.; Jia, Y.; Liu, X.; Zhong, Q. Selective catalytic oxidation of NO with O_2 over Ce-doped MnOx/TiO_2 catalysts. *J. Nat. Gas Chem.* **2012**, *21*, 17–24. [CrossRef]
26. Ma, Z.; Yang, H.; Li, Q.; Zheng, J.; Zhang, X. Catalytic reduction of NO by NH_3 over Fe–Cu–Ox/CNTs-TiO_2 composites at low temperature. *Appl. Catal. A Gen.* **2012**, *427–428*, 43–48. [CrossRef]
27. Shi, Y.; Chen, S.; Sun, H.; Shu, Y.; Quan, X. Low-temperature selective catalytic reduction of NOx with NH_3 over hierarchically macro-mesoporous Mn/TiO_2. *Catal. Commun.* **2013**, *42*, 10–13. [CrossRef]
28. Gao, F.; Tang, X.; Yi, H.; Chu, C.; Li, N.; Li, J.; Zhao, S. In-situ DRIFTS for the mechanistic studies of NO oxidation over α-MnO_2, β-MnO_2 and γ-MnO_2 catalysts. *Chem. Eng. J.* **2017**, *322*, 525–537. [CrossRef]
29. Gao, Y.; Luan, T.; Zhang, W.; Li, H. The promotional effects of cerium on the catalytic properties of Al_2O_3-supported MnFeOx for NO oxidation and fast SCR reaction. *Res. Chem. Intermed.* **2018**, in press. [CrossRef]
30. Pérez Vélez, R.; Ellmers, I.; Huang, H.; Bentrup, U.; Schünemann, V.; Grünert, W.; Brückner, A. Identifying active sites for fast NH_3-SCR of NO/NO_2 mixtures over Fe-ZSM-5 by operando EPR and UV–vis spectroscopy. *J. Catal.* **2014**, *316*, 103–111. [CrossRef]
31. Gong, P.; Xie, J.; Fang, D.; Han, D.; He, F.; Li, F.; Qi, K. Effects of surface physicochemical properties on NH_3-SCR activity of MnO_2 catalysts with different crystal structures. *Chin. J. Catal.* **2017**, *38*, 1925–1934. [CrossRef]
32. Boningari, T.; Pappas, D.K.; Ettireddy, P.R.; Kotrba, A.; Smirniotis, P.G. Influence of SiO_2 on M/TiO_2 (M = Cu, Mn, and Ce) Formulations for Low-Temperature Selective Catalytic Reduction of NOx with NH_3: Surface Properties and Key Components in Relation to the Activity of NOx Reduction. *Ind. Eng. Chem. Res.* **2015**, *54*, 2261–2273. [CrossRef]

33. Luo, S.; Zhou, W.; Xie, A.; Wu, F.; Yao, C.; Li, X.; Zuo, S.; Liu, T. Effect of MnO_2 polymorphs structure on the selective catalytic reduction of NOx with NH_3 over TiO_2–Palygorskite. *Chem. Eng. J.* **2016**, *286*, 291–299. [CrossRef]
34. Jiang, H.; Wang, C.; Wang, H.; Zhang, M. Synthesis of highly efficient MnOx catalyst for low-temperature NH_3-SCR prepared from Mn-MOF-74 template. *Mater. Lett.* **2016**, *168*, 17–19. [CrossRef]
35. Cheng, X.; Zhang, X.; Su, D.; Wang, Z.; Chang, J.; Ma, C. NO reduction by CO over copper catalyst supported on mixed CeO_2 and Fe_2O_3: Catalyst design and activity test. *Appl. Catal. B Environ.* **2018**, *239*, 485–501. [CrossRef]
36. Stanciulescu, M.; Caravaggio, G.; Dobri, A.; Moir, J.; Burich, R.; Charland, J.P.; Bulsink, P. Low-temperature selective catalytic reduction of NOx with NH_3 over Mn-containing catalysts. *Appl. Catal. B Environ.* **2012**, *123–124*, 229–240. [CrossRef]
37. Kong, F.; Qiu, j.; Liu, H.; Zhao, R.; Zeng, H. Effect of NO/SO_2 on Elemental Mercury Adsorption by Nano-Fe_2O_3. *Proc. CSEE (China)* **2010**, *30*, 43–48.
38. Cao, L.; Chen, L.; Wu, X.; Ran, R.; Xu, T.; Chen, Z.; Weng, D. TRA and DRIFTS studies of the fast SCR reaction over CeO_2/TiO_2 catalyst at low temperatures. *Appl. Catal. A Gen.* **2018**, *557*, 46–54. [CrossRef]
39. Jin, R.; Liu, Y.; Wu, Z.; Wang, H.; Gu, T. Low-temperature selective catalytic reduction of NO with NH_3 over MnCe oxides supported on TiO_2 and Al_2O_3: A comparative study. *Chemosphere* **2010**, *78*, 1160–1166. [CrossRef] [PubMed]
40. Ma, L.; Seo, C.Y.; Nahata, M.; Chen, X.; Li, J.; Schwank, J.W. Shape dependence and sulfate promotion of CeO_2 for selective catalytic reduction of NOx with NH_3. *Appl. Catal. B Environ.* **2018**, *232*, 246–259. [CrossRef]
41. Xiong, Z.-B.; Liu, J.; Zhou, F.; Liu, D.-Y.; Lu, W.; Jin, J.; Ding, S.-F. Selective catalytic reduction of Nox with NH_3 over iron-cerium-tungsten mixed oxide catalyst prepared by different methods. *Appl. Surf. Sci.* **2017**, *406*, 218–225. [CrossRef]
42. Liu, F.; He, H.; Zhang, C.; Shan, W.; Shi, X. Mechanism of the selective catalytic reduction of NOx with NH_3 over environmental-friendly iron titanate catalyst. *Catal. Today* **2011**, *175*, 18–25. [CrossRef]
43. Fan, X.; Qiu, F.; Yang, H.; Tian, W.; Hou, T.; Zhang, X. Selective catalytic reduction of NOX with ammonia over Mn–Ce–Ox/TiO_2-carbon nanotube composites. *Catal. Commun.* **2011**, *12*, 1298–1301. [CrossRef]
44. Guan, D.S.; Wang, Y. Synthesis and growth mechanism of multilayer TiO_2 nanotube arrays. *Nanoscale* **2012**, *4*, 2968–2977. [CrossRef] [PubMed]
45. Lu, X.; Shen, C.; Zhang, Z.; Barrios, E.; Zhai, L. Core–Shell Composite Fibers for High-Performance Flexible Supercapacitor Electrodes. *ACS Appl. Mater. Interfaces* **2018**, *10*, 4041–4049. [CrossRef] [PubMed]
46. Wang, C.; Yu, F.; Zhu, M.; Wang, X.; Dan, J.; Zhang, J.; Cao, P.; Dai, B. Microspherical MnO_2-CeO_2-Al_2O_3 mixed oxide for monolithic honeycomb catalyst and application in selective catalytic reduction of NOx with NH_3 at 50–150 °C. *Chem. Eng. J.* **2018**, *346*, 182–192. [CrossRef]
47. Kapteijn, F.; Singoredjo, L.; Andreini, A.; Moulijn, J.A. Activity and selectivity of pure manganese oxides in the selective catalytic reduction of nitric oxide with ammonia. *Appl. Catal. B Environ.* **1994**, *3*, 173–189. [CrossRef]
48. Gao, G.; Shi, J.-W.; Liu, C.; Gao, C.; Fan, Z.; Niu, C. Mn/CeO_2 catalysts for SCR of NOx with NH_3: Comparative study on the effect of supports on low-temperature catalytic activity. *Appl. Surf. Sci.* **2017**, *411*, 338–346. [CrossRef]
49. Zhang, W.; Wang, F.; Li, X.; Liu, Y.; Liu, Y.; Ma, J. Fabrication of hollow carbon nanospheres introduced with Fe and N species immobilized palladium nanoparticles as catalysts for the semihydrogenation of phenylacetylene under mild reaction conditions. *Appl. Surf. Sci.* **2017**, *404*, 398–408. [CrossRef]
50. Wang, T.; Wan, Z.; Yang, X.; Zhang, X.; Niu, X.; Sun, B. Promotional effect of iron modification on the catalytic properties of Mn-Fe/ZSM-5 catalysts in the Fast SCR reaction. *Fuel Process. Technol.* **2018**, *169*, 112–121. [CrossRef]
51. Hu, H.; Cai, S.; Li, H.; Huang, L.; Shi, L.; Zhang, D. Mechanistic Aspects of deNOx Processing over TiO_2 Supported Co–Mn Oxide Catalysts: Structure–Activity Relationships and In Situ DRIFTs Analysis. *ACS Catal.* **2015**, *5*, 6069–6077. [CrossRef]
52. Li, K.; Tang, X.; Yi, H.; Ning, P.; Kang, D.; Wang, C. Low-temperature catalytic oxidation of NO over Mn–Co–Ce–Ox catalyst. *Chem. Eng. J.* **2012**, *192*, 99–104. [CrossRef]

53. Qi, G.; Yang, R.T. Performance and kinetics study for low-temperature SCR of NO with NH_3 over MnOx–CeO_2 catalyst. *J. Catal.* **2003**, *217*, 434–441. [CrossRef]
54. Huang, B.; Yu, D.; Sheng, Z.; Yang, L. Novel CeO_2@TiO_2 core–shell nanostructure catalyst for selective catalytic reduction of NOx with NH_3. *J. Environ. Sci.* **2017**, *55*, 129–136. [CrossRef] [PubMed]
55. Boningari, T.; Somogyvari, A.; Smirniotis, P.G. Ce-Based Catalysts for the Selective Catalytic Reduction of NOx in the Presence of Excess Oxygen and Simulated Diesel Engine Exhaust Conditions. *Ind. Eng. Chem. Res.* **2017**, *56*, 5483–5494. [CrossRef]
56. Ruggeri, M.P.; Grossale, A.; Nova, I.; Tronconi, E.; Jirglova, H.; Sobalik, Z. FTIR in situ mechanistic study of the NH_3NO/NO_2 "Fast SCR" reaction over a commercial Fe-ZSM-5 catalyst. *Catal. Today* **2012**, *184*, 107–114. [CrossRef]
57. Huang, T.-J.; Zhang, Y.-P.; Zhuang, K.; Lu, B.; Zhu, Y.-W.; Shen, K. Preparation of honeycombed holmium-modified Fe-Mn/TiO_2 catalyst and its performance in the low temperature selective catalytic reduction of NOx. *J. Fuel Chem. Technol.* **2018**, *46*, 319–327. [CrossRef]
58. Marbán, G.; Valdés-Solís, T.; Fuertes, A.B. Mechanism of low-temperature selective catalytic reduction of NO with NH_3 over carbon-supported Mn_3O_4: Role of surface NH_3 species: SCR mechanism. *J. Catal.* **2004**, *226*, 138–155. [CrossRef]
59. Wang, J.; Yi, H.; Tang, X.; Zhao, S.; Gao, F.; Yang, Z. Oxygen plasma-catalytic conversion of NO over MnOx: Formation and reactivity of adsorbed oxygen. *Catal. Commun.* **2017**, *100*, 227–231. [CrossRef]
60. Wang, T.; Zhang, X.; Liu, J.; Liu, H.; Guo, Y.; Sun, B. Plasma-assisted catalytic conversion of NO over Cu-Fe catalysts supported on ZSM-5 and carbon nanotubes at low temperature. *Fuel Process. Technol.* **2018**, *178*, 53–61. [CrossRef]